



## Strong pinning in very fast grown reactive co-evaporated GdBa<sub>2</sub>Cu<sub>3</sub>O<sub>7</sub> coated conductors

J. L. MacManus-Driscoll, M. Bianchetti, A. Kursumovic, G. Kim, W. Jo, H. Wang, J. H. Lee, G. W. Hong, and S. H. Moon

Citation: *APL Mater.* **2**, 086103 (2014); doi: 10.1063/1.4893339

View online: <http://dx.doi.org/10.1063/1.4893339>

View Table of Contents: <http://scitation.aip.org/content/aip/journal/aplmater/2/8?ver=pdfcov>

Published by the [AIP Publishing](#)

---

### Articles you may be interested in

[A close correlation between nanostructure formations and the thickness dependence of the critical current density in pure and BaSnO<sub>3</sub>-added GdBa<sub>2</sub>Cu<sub>3</sub>O<sub>7-δ</sub> films](#)

*J. Appl. Phys.* **115**, 163901 (2014); 10.1063/1.4872264

[Thickness dependence of critical current density in GdBa<sub>2</sub>Cu<sub>3</sub>O<sub>7-δ</sub> thin films with BaSnO<sub>3</sub> addition](#)

*J. Appl. Phys.* **111**, 07D714 (2012); 10.1063/1.3676618

[Enhanced flux pinning of air-processed Gd Ba<sub>2</sub> Cu<sub>3</sub> O<sub>7-δ</sub> superconductors with addition of Zr O<sub>2</sub> nanoparticles](#)

*Appl. Phys. Lett.* **89**, 192508 (2006); 10.1063/1.2387863

[Epitaxial nanostructure and defects effective for pinning in Y \( RE \) Ba<sub>2</sub> Cu<sub>3</sub> O<sub>7-x</sub> coated conductors](#)

*Appl. Phys. Lett.* **87**, 132502 (2005); 10.1063/1.2061874

[Strong pinning in ternary \( Nd-Sm-Gd \) Ba<sub>2</sub> Cu<sub>3</sub> O<sub>y</sub> superconductors](#)

*Appl. Phys. Lett.* **80**, 1016 (2002); 10.1063/1.1447582

---

**NEW**  
**7400-S Series**  
Vibrating Sample  
Magnetometers

Lake Shore  
CRYOTRONICS

Ideal for the most demanding  
characterization applications

Learn more

## Strong pinning in very fast grown reactive co-evaporated $\text{GdBa}_2\text{Cu}_3\text{O}_7$ coated conductors

J. L. MacManus-Driscoll,<sup>1,a</sup> M. Bianchetti,<sup>1</sup> A. Kursumovic,<sup>1</sup> G. Kim,<sup>2</sup> W. Jo,<sup>2</sup> H. Wang,<sup>3</sup> J. H. Lee,<sup>3</sup> G. W. Hong,<sup>4</sup> and S. H. Moon<sup>5</sup>

<sup>1</sup>*Department of Materials Science and Metallurgy, University of Cambridge, Cambridge CB2 3QZ, United Kingdom*

<sup>2</sup>*Department of Physics, Ewha Womans University, Seoul 120-750, South Korea*

<sup>3</sup>*Materials Science and Engineering Program, Texas A&M University, College Station, Texas 77843, USA*

<sup>4</sup>*Graduate School of Knowledge Based-Technology and Energy, Korea Polytechnic University, Gyeonggi-do 429-793, South Korea*

<sup>5</sup>*SuNAM Co. Ltd, Ansong, Gyeonggi-Do 430-817, South Korea*

(Received 11 June 2014; accepted 6 August 2014; published online 22 August 2014)

We report on compositional tuning to create excellent field-performance of  $J_c$  in “self-doped,”  $\text{GdBa}_2\text{Cu}_3\text{O}_{7-y}$  (GdBCO) coated conductors grown by ultrafast reactive co-evaporation. In order to give excess liquid and  $\text{Gd}_2\text{O}_3$ , the overall compositions were all Ba-poor and Cu-rich compared to GdBCO. The precise composition was found to be critical to the current carrying performance. The most copper-rich composition had an optimum self-field  $J_c$  of  $3.2 \text{ MA cm}^{-2}$ . A more Gd-rich composition had the best in-field performance because of the formation of low coherence, splayed  $\text{Gd}_2\text{O}_3$  nanoparticles, giving  $J_c$  (77 K, 1 T) of over  $1 \text{ MA cm}^{-2}$  and  $J_c$  (77 K, 5 T) of over  $0.1 \text{ MA cm}^{-2}$ . © 2014 Author(s). All article content, except where otherwise noted, is licensed under a Creative Commons Attribution 3.0 Unported License. [<http://dx.doi.org/10.1063/1.4893339>]

For many years, the evaporation method has been studied widely for the manufacture of high quality 2G coated conductors on large scales with a high production rate.<sup>1,2</sup> Reactive co-evaporation by cyclic deposition and reaction (RCE-CDR) is a very promising method for coated conductor production. Low oxygen partial pressure ( $p\text{O}_2$ ) is used for the deposition followed by reaction in high  $p\text{O}_2$ , in a cyclic manner.<sup>3,4</sup> However, this system is complex and incurs high labour or equipment depreciation costs and it is difficult to scale-up. On the other hand, reactive co-evaporation by deposition and reaction (RCE-DR) is simpler and has significantly higher deposition rates by around an order of magnitude (the conversion from an amorphous glassy phase to a superconducting phase occurs at high temperature and high oxygen pressure very quickly, within around 30 s).<sup>5-7</sup> The process involves moving through a liquid phase zone before conversion of these phases to the superconducting phase. It is possible to make  $\sim 1 \text{ km}$  length conductors in only 2–5 h<sup>8,9</sup> with critical currents in excess of  $450 \text{ A cm}^{-1}$  at 77 K.

For some applications of coated conductors it is necessary to optimize  $J_c$  at low fields (e.g., for fault current limiters), whereas for others (e.g., motors or magnet inserts) it is necessary to optimize  $J_c$  for higher fields. In the RCE-DR process, the fraction of liquid and excess rare earth pinning fraction depend critically on the precursor composition, and it is important to determine how precursor composition influences the  $J_c(H)$  behaviour. We address this question in this study.

Figure 1(a) shows a schematic image of the batch-type RCE-DR system and the crucial parameters of the process are shown in Table I. The system consists of two different parts: a multi-turn reel-to-reel (R2R) deposition chamber and a reaction zone. Films are first

<sup>a</sup>Email: [jld35@cam.ac.uk](mailto:jld35@cam.ac.uk)



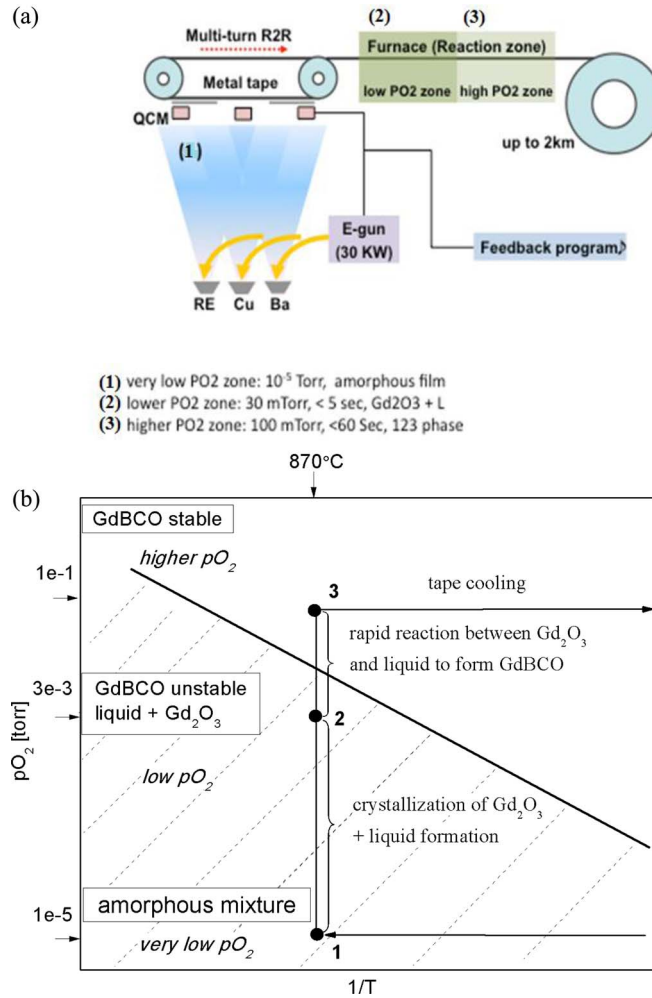


FIG. 1. (a) Schematic of the Reactive Co-Evaporation-Deposition and Reaction (RCE-DR) method employed by SUNAM for making long length GdBCO conductors. (b) The growth path followed during the reactive co-evaporation deposition and reaction (RCE-DR) method employed by SUNAM superimposed on the GdBCO phase stability line. The position of the line is not well documented and hence is only schematic here. Note that this plot is applicable to films of GdBCO and hence the decomposition phases are different to the bulk, e.g., Gd<sub>2</sub>BaCuO<sub>5</sub> is not apparent when GdBCO decomposes at either high T or low pO<sub>2</sub> or both. Instead Gd<sub>2</sub>O<sub>3</sub> is formed owing to epitaxial stabilization of this phase.

TABLE I. Parameters for growth of long length HTS conductor by the Reactive Co-Evaporation-Deposition and Reaction (RCE-DR) method employed by SUNAM.

Parameter	Process parameters
Raw material	Bulk (cheap metal material)
T <sub>s</sub>	870 °C
pO <sub>2</sub> zone	1: ~10 <sup>-5</sup> Torr, lower zone 2: ~30 mTorr, higher zone 3: 100 mTorr
Deposition rate	Total: ~ 1.0 km in 2–5 h, Fast (~30 s) conversion
E-beam power	Fix 30 kW of each material
Vacuum	Differential pumping channel between reel to reel and heat treatment regions

deposited in the deposition chamber on a ~50 nm LaMnO<sub>3</sub> (LMO) buffered IBAD-MgO hastelloy metal tape<sup>10</sup> at a deposition rate of 0.1 μm/min with multi pass deposition and translation rate of 120 m/h, at a very low partial oxygen pressure around 10<sup>-5</sup> Torr.<sup>9,11</sup> Each metallic component evaporation rate is controlled by a quartz crystal monitor and feedback program. Each material was put in a crucible, and deposited with a differentially pumped pierce type e-gun (30 kW). 10 m length

TABLE II. Compositions of the three samples studied and the microstructural and superconducting properties achieved.

Film	Thickness ( $\mu\text{m}$ )	$I_c$ (12 mm-width, A)	$J_c$ (77 K self-field, $\text{MA}/\text{cm}^2$ )	$T_c$ (K)	Atomic ratio (Gd:Ba:Cu)	Gd/(Ba+Cu)	Comment on composition	$\Delta\phi^\circ$	$\Delta\omega^\circ$
						Calculated based on the position of composition on L+ $\text{Gd}_2\text{O}_3$ tie line			
A	1	185	1.54	92.47	1.0:0.88:3.04	0.255	Most Gd-rich/liquid poor	4.92	2.66
B	1.15	334	2.42	92.22	1.0:1.25:3.42	0.215	Intermediate Gd and liquid	4.36	2.93
C	1.14	440	3.21	92.82	1.0:1.09:5.32	0.156	Most liquid-rich/Gd poor	4.16	2.25

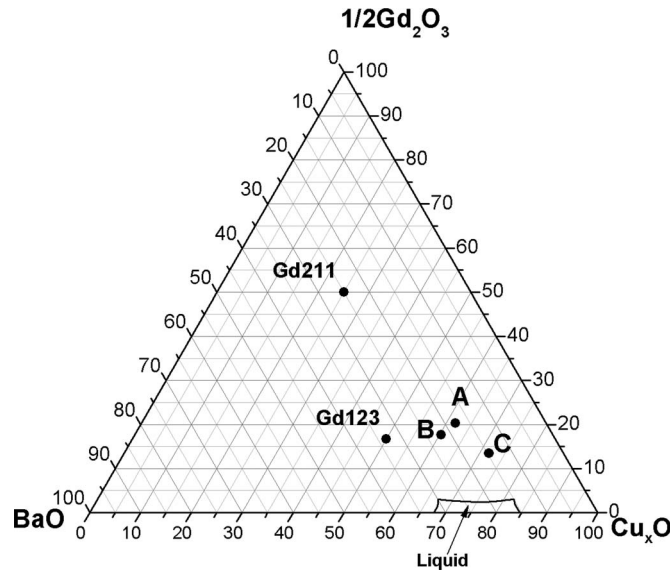


FIG. 2. Ternary phase diagram showing the positions of compositions studied in this work. As discussed in the main text, the position of the liquid region is schematic, and is based on Ref. 16. All compositions A, B, and C lie on the tie line, “ $1/2\text{Gd}_2\text{O}_3 + \text{liquid}$ ” and hence when in region 2 of Fig. 1, only these phases are present.

conductors were fabricated in around 5 min and pieces were cut from this length for the various measurements.

Figure 1(b) shows a schematic phase stability diagram and the path followed for the conversion process through the  $\text{GdBa}_2\text{Cu}_3\text{O}_{7-y}$  (GdBCO) phase stability diagram.<sup>12</sup> The diagram is schematic because the conversion process is not undertaken at equilibrium. We also note that the GdBCO line position is not identical to the  $\text{YBa}_2\text{Cu}_3\text{O}_{7-y}$  (YBCO) line because different rare earths shift the stability lines quite considerably.<sup>13</sup> After deposition of the precursor, the tape is moved from the very low  $p\text{O}_2$  zone (Region 1,  $\sim 10^{-2}$  mTorr  $\text{O}_2$ ) where an amorphous phase (with possibly some nanocrystalline regions) is present, to the low  $p\text{O}_2$  zone (Region 2,  $\sim 30$  mTorr) where nanocrystalline  $\text{Gd}_2\text{O}_3$  forms. While bulk equilibrium thermodynamics predicts  $\text{Gd}_2\text{BaCuO}_5$  to be stable in region 2,  $\text{Gd}_2\text{O}_3$  is stable instead owing to reduced kinetics and/or epitaxial driving forces.<sup>14</sup> Finally, in the higher  $p\text{O}_2$  zone (Region 3,  $\sim 100$  mTorr), GdBCO forms very rapidly ( $< 60$  s).

Up to now, a typical ratio of Gd:Ba:Cu of  $\sim 1:1:2.5$  has been studied.<sup>9,15</sup> However, here, to give a higher liquid fraction during processing, we explore 3 new Cu-rich compositions (A, B, C) as shown in Table II and in Figure 2. The position of the liquid region in Figure 2 is schematic. The region is not well documented for low  $p\text{O}_2$ 's. We have estimated the position of the liquid region based on the work of Wong-Ng and Cook.<sup>16</sup> A summary of the compositions of the 3 samples studied is as follows:

- A is the most Gd-rich and (Ba+Cu) poor. It is therefore furthest away from the liquid region of Fig. 2. It is the most  $\text{Gd}_2\text{O}_3$ -rich and liquid-poor composition.

- B is the intermediate composition where both moderate  $\text{Gd}_2\text{O}_3$  and liquid are present.
- C is the most Gd-poor and hence most (Ba+Cu) rich. It is therefore the most  $\text{Gd}_2\text{O}_3$ -poor and liquid-rich composition.

All compositions lie on quasi-equilibrium “L+ $\text{Gd}_2\text{O}_3$ ” tie lines (to avoid confusion these lines are not shown in Fig. 2). Hence, for all three compositions, *only*  $1/2\text{Gd}_2\text{O}_3$  and L should be present at stage 2 of the processing stage (before conversion to GdBCO), as shown both in Figs. 1(a) and 1(b). During the conversion to GdBCO, i.e., moving to region 3 of Fig. 1(b), the GdBCO crystallizes and the liquid moves to the surface of the film.<sup>17</sup> After the conversion is complete, “GdBCO ( $\text{Gd}_{123}$ ) +  $1/2\text{Gd}_2\text{O}_3$  + solidified liquid” should be present in proportions roughly determined from the phase diagram of Fig. 2. The “solidified liquid” at the film surface is in the form of  $\text{BaCuO}_2$  +  $\text{Cu}_2\text{O}$ .<sup>12</sup>

The microstructural and superconducting properties of a number of  $\sim 1$  cm sections of tape cut from each length were studied. There was a high reproducibility of all measured properties along the tape length. X-ray diffraction (XRD) ( $\theta$ - $2\theta$  scans and  $\phi$  scans) was undertaken to learn about the crystallinity and misorientation of the grains. Low resolution and high resolution cross sectional transmission electron microscopy (TEM) were undertaken to image the microstructural features in the tapes.

The transport critical current density was measured at 77 K using a conventional four-point probe method with a  $1 \mu\text{V cm}^{-1}$  criterion on  $50 \mu\text{m}$  wide bridges. Using a photolithographic technique, resist pads were transferred on the electrical contact area of the sample and a solution of  $\text{H}_2\text{O}_2$ ,  $\text{NH}_3$ , and ethanol was used to remove the unprotected silver capping layer from the sample and expose the GdBCO layer. Similarly, resist track patterns were transferred on the GdBCO surface and the unprotected GdBCO layer was removed using ion milling process and wet etching. The transition temperature ( $T_c$ ), the critical current density field dependency ( $J_c(B)$ ), and the angular dependency ( $J_c(\theta)$ ) in maximum Lorentz force configuration by rotating the applied magnetic field in a plane perpendicular to the current direction were all measured.

X-ray diffraction of the tapes showed all the expected ( $00l$ ) peaks for the different materials present in the metallic tape, buffer, and film (see Figure S1(a) in the supplementary material<sup>24</sup>). ( $00l$ )  $\text{Gd}_2\text{O}_3$  was present owing to its formation in Region B of the growth diagram (Figure 1(b)) and ( $111$ )  $\text{Cu}_2\text{O}$ , ( $600$ )  $\text{BaCuO}_2$ , and ( $211$ )  $\text{BaCu}_2\text{O}_2$  were present because it forms when remnant liquid phase solidifies. Figures S1(b) and S1(c) in the supplementary material<sup>24</sup> show the rocking curves and  $\phi$  scans of the different samples, and the  $\Delta\phi$  and  $\Delta\omega$  values extracted from these plots are included in Table II.

Summarizing the relationship between the microstructure and superconducting properties of the different samples, we find:

- Sample A has the highest in-plane grain misorientation ( $\Delta\phi = 4.92^\circ$ ) and the lowest  $J_c$  of  $1.54 \text{ MA cm}^{-2}$ . This is expected since grain orientation and self-field  $J_c$  are closely connected.<sup>18</sup> The large in-plane misorientation likely results from the lower amount of liquid present in the sample, which means less kinetic assistance to align the GdBCO grains with respect to one another during the rapid conversion process.
- Sample B of intermediate composition has an intermediate self-field  $J_c$  of  $2.42 \text{ MA cm}^{-2}$  and an intermediate  $\Delta\phi$  of  $4.36^\circ$ , and the best in-field  $J_c$  performance.
- Sample C shows the opposite behavior to A. It has the highest liquid fraction, the lowest in-plane grain misorientation ( $\Delta\phi = 4.16^\circ$ ), and the highest self-field  $J_c$  of  $3.21 \text{ MA cm}^{-2}$ .

To understand about the pinning in the different samples, we now turn to the in-field  $J_c$  performance. Figure 3 shows representative data from 1 cm sections from each sample composition. As noted already, within each composition batch there was very little difference between each section measured. The first observation of Fig. 3 is that sample B shows a very similar form of in-field performance as sample A, both with only a gradual drop-off of  $J_c$  at higher fields. However, the overall levels of the  $J_c(H)$  are different with B being shifted up compared to A. The result indicates that the difference in liquid fraction (more in B than A, see Table II) is more critical to the self-field  $J_c$  than the difference in  $\text{Gd}_2\text{O}_3$  fraction (less in B than A) is to the  $c$ -axis pinning. The second

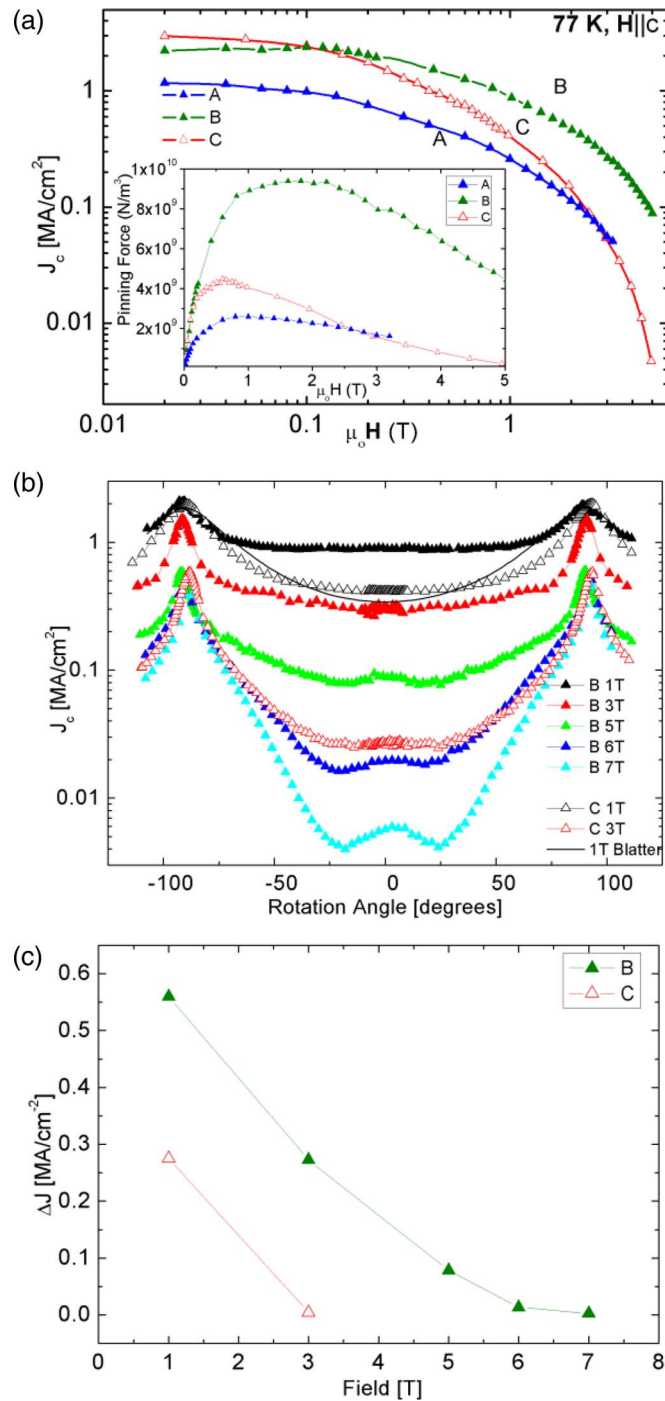


FIG. 3.  $J_c$  measurements. (a)  $J_c$  versus  $H$  parallel to  $c$  for samples A, B, and C. Inset shows pinning force versus field for the 3 samples; (b) Angular  $J_c$  data comparing samples B and C; (c)  $\Delta J$  (defined as the difference between the experimental value and the random pinning contribution obtained via the Blatter model fitting) versus field parallel to  $c$  comparing samples B and C.

observation is that there is a worse field dependence of  $J_c$  for sample C compared to samples A and B. This is consistent with there being significantly less Gd (and hence less  $Gd_2O_3$  pinning phase) and more liquid in C. Less  $Gd_2O_3$  and more liquid will mean a greater possibility of more ripening of the lower  $Gd_2O_3$  fraction during the conversion process. We discuss this point more later when we analyse the TEM data.

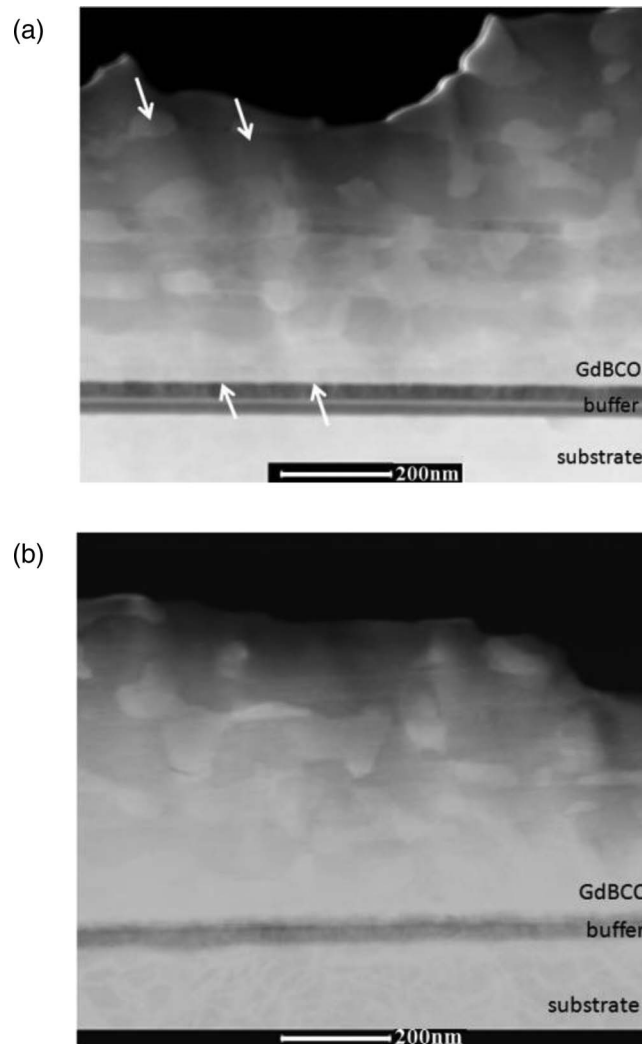


FIG. 4. Cross-sectional TEM images of samples B (a) and C (b). For B,  $\text{Gd}_2\text{O}_3$  nanoparticles are present in the film and they show, splayed low coherence along  $c$  as indicated by the 2 sets of arrows. For C, the  $\text{Gd}_2\text{O}_3$  nanoparticles are more random without any apparent orientation along  $c$ .

The key point that comes out of Fig. 3(a) is that precise tuning of the Gd to liquid fraction ratio is very important to the conductor performance. On the other hand, for the RCE-DR process, this result is perhaps not surprising considering the very rapid speed of phase formation in the conversion process and it indicates that precise control of the precursor composition is very important.

Looking now in more detail into the pinning of the three samples using pinning force plots (inset to Fig. 3(a)), we find that A has a low, very broad peak with maximum pinning force  $Fp_{max}$  at  $\sim 0.8$  T; B has a much larger and broader peak with  $Fp_{max}$  at  $\sim 1.8$  T; and C has a small peak with  $Fp_{max}$  at  $\sim 0.6$  T. The difference in the curves clearly shows the very different pinning landscapes resulting from the compositional variation, with the most effective pinning coming from sample B of intermediate Gd:liquid ratio.

We then focused on understanding the reasons for the different performances of the samples. We focused on comparing the best in-field performance sample (sample B) to the best self-field performance (sample C). Field angular measurements of  $J_c$  (Figs. 3(b) and 3(c)) and TEM (Fig. 4) analyses were undertaken. Looking first at the angular data (Fig. 3(b)), we find that at any given field B has higher  $J_c$  values over all angles than C (sample C was measured to only 3 T since above this field  $J_c$  dropped off rapidly). For sample B, between the  $\theta = 90^\circ$  (ab) peaks, a very broad, flat

region of  $J_c$  is observed, indicative of a smeared  $c$  axis peak. This flat region is much less obvious for sample C.

To extract the  $c$  axis component of  $J_c$  from the angular data, the curves were fitted according to Blatter's anisotropic scaling approach.<sup>19</sup> According to this model, the  $J_c$ 's of samples with uncorrelated point-like disorder depends only on a single variable  $\hat{H} = H(\cos(\Theta)^2 + \gamma^{-2}\sin(\Theta)^2)$ , where  $\gamma \sim 5-7$  is the electronic mass anisotropy. Thus, the measured  $J_c(\Theta, H)$  curves collapse together in the  $(\Theta, H)$  regions where only random pinning is present when plotted as a function of  $\hat{H}$ . In this case  $\gamma$  is a fitting parameter constrained to the values 5-7. The collapsed curve  $J'(\hat{H})$  represents the random pinning contribution to  $J_c(\Theta, H)$  and can be mapped back to the experimental data. The difference,  $\Delta J$ , between  $J_c$  and  $J'$  is the contribution of correlated pinning to  $J_c$  given by the *combined* effect of random and correlated random pinning.

Figure 3(c) shows  $\Delta J$  versus field for both samples. The values are much larger for B than for C and the data for B also extend to higher fields (6 T compared to  $\sim 3$  T). Hence, for sample B strong  $c$  axis correlated pinning is observed at all fields. The width of the  $c$  axis peak for B (not shown) was large, approximately  $\sim 150^\circ$ , indicative of splayed, low coherence nanoparticles along the  $c$ -axis. This is similar to what is observed in RE<sub>2</sub>O<sub>3</sub> excess Metal Organic Deposition (MOD) conductors Ref. 20. The difference though is that the conversion process using the RCE-DR process is much faster than the MOD process. Also, strong  $c$  axis pinning is not common for growth processes which involve a large liquid excess fraction. Growth in the presence of excess liquid normally leads to low pinning Refs. 21 and 22 because of high crystalline perfection. On the other hand, for the RCE-DR process the growth is very fast and so defects are not healed out by the liquid. There are similarities both in the nature of the process and in the properties obtained to the hybrid liquid phase epitaxy process for making coated conductors Ref. 23.

An understanding of the different pinning exhibited by B and C is gained from cross-sectional TEM images (Fig. 4). For sample B (Fig. 4(a)), we observe low coherence regions of rather equiaxed nanoparticles of Gd<sub>2</sub>O<sub>3</sub> with alignment broadly along the  $c$ -axis (examples are indicated by two sets of arrows) and with spacing between  $\sim 50$  nm and 100 nm, corresponding to a matching field of  $\sim 1-2$  T. Wide possible tilt angles were observed which mimic a broad splay of defect correlations. The TEM data are consistent with the various  $J_c$  data of Figs. 3(a)-3(c).

Nanoparticles of Gd<sub>2</sub>O<sub>3</sub> are also present in sample C (Figure 4(b)) but they show no clear tilt alignment along  $c$  and are therefore considered to act mainly as random defects. This explains both the lower  $c$  axis peak in the angular data (Figures 3(b) and 3(c)) and the poorer field dependence (Figure 3(a)) observed for sample C. The nanoparticles are also slightly larger and appear more fused together than for sample B, consistent with the presence of a larger liquid phase fraction in C (Table II).

Although it was not possible to accurately assess from TEM or XRD the relative fractions of Gd<sub>2</sub>O<sub>3</sub> between samples B and C, the higher out-of-plane grain tilting ( $\omega$ ) of B compared to C ( $\Delta\omega = 2.93^\circ$  and  $2.25^\circ$ , respectively, Table II) is consistent with both more Gd<sub>2</sub>O<sub>3</sub> nanoparticles which disturb the growth of the GdBCO grains, and less liquid to assist the alignment of the GdBCO grains during growth. It should be noted though that for both samples B and C, despite the very fast growth process, from TEM the Gd<sub>2</sub>O<sub>3</sub> nanoparticles were observed to grow heteroepitaxially within the GdBCO matrix without any major disturbance of the surrounding GdBCO lattice. A high-resolution cross sectional TEM for sample C is shown in Figure S2(a) of the supplementary material.<sup>24</sup>

Finally, it is important to note that the interface of GdBCO with IBAD MgO is very clean (see Figure S2(b) of the supplementary material<sup>24</sup>) indicating no destruction of the buffer by the presence of the large amount of liquid. This is very important for production of long length conductors where no weak spots by corrosion of the buffer or metal by the liquid can be tolerated anywhere along the length. In normal circumstances of growth in the presence of a large amount of liquid, the buffer is attacked by the liquid,<sup>17</sup> but the special feature of the rapidity of the RCE-DR conversion process means this is not the case.

The superconducting and microstructural properties of GdBa<sub>2</sub>Cu<sub>3</sub>O<sub>7</sub> coated conductors fabricated by an ultrafast RCE-DR process were studied. Three new precursor compositions were explored which were Ba-poor and Cu-rich compared to the 1:2:3 ratio, and which were more Cu-rich than in previous studies. The conductor performance was found to be strongly dependent on

the precise composition. The best conductor in terms of in-field performance had an intermediate Gd:Ba:Cu ratio (1.0:1.25:3.42). The conductor contained heteroepitaxial Gd<sub>2</sub>O<sub>3</sub> nanoparticles which had a broad splay of defect correlations with wide possible tilt angles. This gave rise to strong and broad correlated pinning around the *c* axis of the GdBCO, with  $J_c$  (77 K, 1 T) of over 1 MA cm<sup>-2</sup> and  $J_c$  (77 K, 5 T) of over 0.1 MA cm<sup>-2</sup>. Creation of this broad coherence of nanoparticles in very rapidly grown conductors is a unique feature of the RCE-DR process and is very promising for achieving high performance conductor at low cost.

J.L.M.-D., M.B., and A.K. acknowledge support of the EU project, Eurotapes, FP7 (2007-2013) under Grant Agreement No. 280432, and the ERC advanced investigator grant, NOVOX, ERC-2009-AfG-247276. We thank Boris Maiorov for discussions about the Blatter anisotropic scaling model and the discussion of the angular data. W. Jo acknowledges the support of QMMRC program from by the National Research Foundation of Korea (NRF) grant funded by the Korea government (MSIP) (No. 2008-0061893).

- <sup>1</sup> R. H. Hammond, Adv. Supercond. VIII, *Proceedings 8th International Symposium Superconductivity (ISS)* (Springer, Hamamatsu, Japan) 1029 (1996).
- <sup>2</sup> J. W. Lee and S. I. Yoo, *Supercond. Cryog.* **14**, 5 (2012).
- <sup>3</sup> R. Nemetschek, W. Prusseit, B. Holzapfel, J. Eickemeyer, B. DeBoer, U. Miller, and E. Maher, *Physica C* **372–376**, 880 (2005).
- <sup>4</sup> V. Matias, E. J. Rowley, Y. Coulter, B. Maiorov, T. Holesinger, C. Yung, V. Glyantsev, and B. Moeckly, *Supercond. Sci. Technol.* **23**, 014018 (2010).
- <sup>5</sup> M. R. Beasley and R. H. Hammond, DOE Annual Report (Award No. DE-FC07-03ID14510), 2005.
- <sup>6</sup> G. Koster, J. Huh, R. H. Hammond, and M. R. Beasley, *Appl. Phys. Lett.* **90**, 261917 (2007).
- <sup>7</sup> M. R. Beasley and R. H. Hammond, Final DOE Scientific/Technical Report 2003–2008. (Award No. DE-FC07-03ID14510), 2009.
- <sup>8</sup> J. W. Lee, J. H. Lee, S. H. Moon, and S. I. Yoo, *Supercond. Cryog.* **14**, 28–31 (2012).
- <sup>9</sup> J. H. Lee, H. Lee, J. W. Lee, S. M. Choi, S. I. Yoo, and S. H. Moon, *Supercond. Sci. Technol.* **27**, 044018 (2014).
- <sup>10</sup> S. S. Oh, H. S. Ha, H. S. Kim, R. K. Ko, K. J. Song, D. W. Ha, T. H. Kim, N. J. Lee, D. Youm, J. S. Yang, H. K. Kim, K. K. Yu, S. H. Moon, K. P. Ko, and S. I. Yoo, *Supercond. Sci. Technol.* **21**, 034003 (2008).
- <sup>11</sup> S. Moon, Private Communication, 2013.
- <sup>12</sup> J. L. MacManus-Driscoll, J. C. Bravman, and R. B. Beyers, *Physica C* **241**, 401 (1995).
- <sup>13</sup> J. A. G. Nelstrop and J. L. MacManus-Driscoll, *Physica C* **377**, 585 (2002).
- <sup>14</sup> T. Ohnishi, J. Huh, R. H. Hammond, and W. Jo, *J. Mater. Res.* **19**, 977 (2004).
- <sup>15</sup> S. M. Choi, J. W. Lee, S. H. Moon, and S. I. Yoo, *Mater. Res. Soc. Symp. Proc.* **2012**, 1434.
- <sup>16</sup> W. Wong-Ng and L. P. Cook, *J. Res. Natl. Inst. Stand. Technol.* **103**, 379 (1998).
- <sup>17</sup> X. Qi, Z. Lockman, Y. Bugoslavsky, A. Kursumovic, R. Tomov, B. A. Glowacki, J. Evetts, and J. L. MacManus-Driscoll, *Supercond. Sci. Technol.* **17**, 1144 (2004).
- <sup>18</sup> D. Dimos, P. Chaudhari, and J. Mannhart, *Phys. Rev. B* **41**, 4038 (1990).
- <sup>19</sup> L. Civale, B. Maiorov, A. Serquis, J. O. Willis, J. Y. Coulter, H. Wan, Q. X. Jia, P. N. Arendt, J. L. MacManus-Driscoll, M. P. Maley, and S. R. Foltyn, *Appl. Phys. Lett.* **84**, 2121 (2004).
- <sup>20</sup> T. G. Holesinger, L. Civale, B. Maiorov, D. M. Feldmann, J. Y. Coulter, D. J. Miller, V. A. Maroni, Z. Chen, D. C. Larbalestier, R. Feenstra, X. Li, Y. Huang, T. Kodanandath, W. Zhang, M. W. Rupich, and A. P. Malozemoff, *Adv. Mater.* **20**, 391 (2008).
- <sup>21</sup> A. Vostner, S. Tonies, H. W. Weber, Y. S. Cheng, A. Kursumovic, J. E. Evetts, S. H. Mennema, and H. W. Zandbergen, *Supercond. Sci. Technol.* **16**, 1152 (2003).
- <sup>22</sup> A. Vostner, Y. F. Sun, H. W. Weber, Y. S. Cheng, A. Kursumović, and J. E. Evetts, *Physica C* **399**, 120 (2003).
- <sup>23</sup> B. Maiorov, A. Kursumovic, L. Stan, H. Zhou, H. Wang, L. Civale, R. Feenstra, and J. L. MacManus-Driscoll, *Supercond. Sci. Technol.* **20**, S223 (2007).
- <sup>24</sup> See supplementary material at <http://dx.doi.org/10.1063/1.4893339> for showing x-ray and cross sectional TEM analyses of the films of this study.